Forsch Ingenieurwes (2022) 86:845–859
https://doi.org/10.1007/s10010-022-00598-8

ORIGINALARBEITEN/ORIGINALS

Fast tooth deflection calculation method and its validation

Jonas-Frederick Hochrein[1] · Michael Otto[1] · Karsten Stahl[1]

Received: 2 March 2022 / Accepted: 30 August 2022 / Published online: 26 September 2022

Abstract

For the development of high power density gearboxes the knowledge of the gear mesh behavior is important. Especially, the tooth deflection influences flank load distribution and is the basis for the design of flank modifications. Analytical and numerical approaches are suitable to evaluate the behavior. Since numerical methods are complex, elaborate and time-consuming, fast and accurate analytical methods are still important and are worth to be further developed and assessed.

An analytical method for calculating tooth deformation for gears goes back to Weber and Banaschek from 1953. In the initial work the final equations are given without many intermediate steps in the plane strain assumption for materials with Poisson's ratio $\nu = 0.3$. This paper derives the tooth deflection equations in a more detailed and general manner for any linear material. The final equations are valid for the plane stress and plane strain state in one new closed representation and are therefore suitable for an efficient implementation. While the plane strain state is typical for gears, the plane stress state is significant for a thin slice model or special gearings. The presented method captures the shear influence with a more detailed calculation of the shear correction factor.

A calculation study validates the results from the derived analytical tooth deflection calculation method with a plane Finite Element Model. In the study the point of application of force and the gear body are varied to cover the influence of different variants (size and mesh position). Finally limits of the analytical modeling and the validation are discussed.

Schnelle Methode zur Berechnung der Zahnverformung und ihre Validierung

Zusammenfassung

Für die Entwicklung von Getrieben mit hoher Leistungsdichte ist die Kenntnis des Eingriffsverhaltens entscheidend. Insbesondere die Zahnverformung beeinflusst die Lastverteilung im Eingriff und ist die Grundlage für die Auslegung von Flankenkorrekturen. Zur Berechnung der Lastverteilung eignen sich analytische und numerische Ansätze. Numerische Methoden sind oftmals komplex, aufwändig und rechenintensiv. Schnelle und genaue analytische Methoden sind daher nach wie vor wertvoll und ihre Weiterentwicklung wertvoll und lohnenswert.

Eine analytische Methode zur Berechnung der Zahnverformung geht auf Weber und Banaschek aus dem Jahr 1953 zurück. Von Ihnen werden die endgültigen Gleichungen ohne viele Zwischenschritte im ebenen Dehnungszustand für Materialien mit einer Poissonzahl von $\nu = 0{,}3$ angegeben. In der vorliegenden Arbeit werden die Gleichungen für die Zahnverformung in einer detaillierteren und allgemeineren Weise für beliebige lineare Materialien hergeleitet. Die finalen Gleichungen gelten für den ebenen Spannungs- und den ebenen Dehnungszustand in einer neuen geschlossenen Darstellung und sind daher für eine effiziente Implementierung geeignet. Der ebene Dehnungszustand ist für Zahnräder typisch. Für ein Scheibchenmodell oder für Sonderverzahnungen ist der ebene Spannungszustand von Bedeutung. Die vorgestellte Methode erfasst den Schubeinfluss durch eine detailliertere Berechnung des Schubkorrekturfaktors.

✉ Jonas-Frederick Hochrein
Jonas.Hochrein@tum.de

[1] TUM School of Engineering and Design, Gear Research Center (FZG), Boltzmannstraße 15, 85748 Garching bei München, Germany

In einer Berechnungsstudie werden die Ergebnisse der analytischen Methode zur Berechnung der Zahnverformung mit einem ebenen Finite-Elemente Modell verglichen und validiert. In der Studie werden der Kraftangriffspunkt und der Zahnradkörper variiert, um den Einfluss verschiedener Varianten (Größe und Eingriffsposition) zu erfassen. Abschließend werden Grenzen der analytischen Modellierung und die Validierung diskutiert.

1 Introduction

Gears are the most commonly used machine elements for transmitting of power. Due to the growing need for lightweight, efficient and noise-optimized transmissions, gears are the subject of constant development and improvement. Teeth deflection between two gears in contact with each other is one essential influence variable in the load capacity calculation [1] and the evaluation of the NVH behavior [2]. The load divided by the tooth deflection defines the linear tooth stiffness, which is the reciprocal value of the tooth compliance. Among the deflection of other gearbox elements (e.g., bearings, shafts, gearbox housing), the tooth deflection defines the contact pattern and therefore the load distribution between two meshing gears. In an iterative process, the load pattern can be used to define flank modifications in order to improve the mesh behavior. In this paper, tooth deflection is defined as the deformation of the tooth and the subsequent gear body. Furthermore, tooth deflection means the macroscopic deformation of the tooth itself. The method in this paper allows to add any contact deformation calculation method of the mating gears and is therefore suitable for the implementation of a modular method. Approaches for the microscopic deformation of two contacting bodies can be found for example in the rolling bearing analysis.

Analytical and numerical methods can be used to calculate tooth deflection. Numerical methods, like the finite element (FE) or boundary element (BE) method, can cover a variety of influences (temperature dependence, nonlinear material behavior, complex geometries ...) but are complex, elaborate and time consuming. In contrast to analytical methods, a lot of effort has to be expended to create, validate and evaluate the model. Bong [3] and Neupert [4, 5] describe a method for calculating the tooth deflection with a 3D FE model under single-point loading. The tooth contact is determined by a geometric relation of the undeformed gears and therefore an input value. They investigate point loading on FE nodes and develop a method to handle the singular effects. Schäfer [6, 7] improves the method for gearings with flank modifications. Vijayakar und Houser [8–10] propose a coupled model for analyzing gears in contact. Contact stress and deformation can be calculated by combining a 3D FE model and the Boussinesq surface integral [11]. Their main focus is to efficiently formulate and solve the 3D contact problem. Similar to the model by Vijayakar und Houser, Guingand [12] describes the deflection calculation of complex tooth geometries by implementing a coupled FE-Boussinesq model. Vedmar [13] develops a 3D FE tooth deflection calculation method based on the superposition principle. The first model calculates the tooth surface contact deformation. A point force is applied to one single tooth on the second model. Subtracting of both parts yields the tooth deflection. Based on the results of a calculation study, Vedmar defines approximative equations for the tooth deflection of gears with common characteristic parameters. Similar to Vedmar, Chang [14] and Feng [15] propose a tooth deflection calculation method based on the superposition of two partial 3D FE models. Their work differs from Vedmar in the sub-modeling and the contact deformation calculation. Beinstingel [16, 17] proposes an isogeometric FE model based on Non-Uniform Rational B-Splines (NURBS) to calculate the tooth deflection. The model shows a good agreement compared to established gear calculation software.

Hybrid methods combine analytical and numerical approaches to calculate the tooth deflection efficiently. In these models usually the total macroscopic tooth deformation is calculated using a numerical method, while the microscopic (contact-) deformation is treated analytically [18, 19]. Most of the numerical approaches presented can be used in a hybrid model. Further hybrid models can be found in the literature. Hong [20] calculates the tooth deflection with the Raleigh-Ritz plate approach by Yau [21] and the gear body deflection following the dimensionless formulas derived by Stegemiller [22] from FE calculations. In Hong's approach the contact deflection is calculated with the Boussinesq surface integral [11]. Rincon [23] and Iglesias [24] describe a two-step FE-based method for calculating global deflection and calculate local deflection using the contact model of Weber and Banaschek [25].

Analytical methods for calculating tooth deflection are not as universal as numerical models. Since the analytical methods are fast and their accuracy does not depend on a specific discretization, they are still important and worth being further developed and assessed. In 1892, Lewis investigated the gear teeth strength using a basic beam model [26]. In 1953, Weber and Banaschek (W/B) [25] calculated the tooth deflection of a plane gear section (transverse section) based on a substitute beam model for the tooth and a substitute half-plane model for the gear body. In their work, the final equations are given without many intermediate steps in the plane strain assumption for materials with Poisson's ratio $\upsilon = 0.3$. Based on the calculation frame-

work established by W/B, Schmidt [27] extends the plane approach in the facewidth direction for spur and helical gears. This is an important extension because the deflection changes over the facewidth depending on the point of load application (cross influence). Therefore, Schmidt calibrates a substitute model of a finite cantilever plate using the tooth deflection postulated by W/B. Schmidt's model is widely used in gear contact and NVH research [28–31]. Using an alternative plate approach, Conry [32, 33] also makes the extension to a finite gear. Another possible way to the extend W/B method is to use the thin slice model. The gear is divided into multiple parallel arranged uncoupled slices. For helical gears, the cuts for the slices are made in normal sections. Therefore, Lutz [34] formulates the W/B tooth substitute model in the plane stress state for worm gears. The substitute model for the gear body remains unaffected. While the plane strain state is used for continuums with one dimension significantly larger than the others (conventional gear model), the plane stress state is suitable for flat continuums (thin slice gear model). In addition, Lutz converts the equations for other materials rather than steel. An improvement in the thin slice model is to couple the single slices. Based on FE calculations, Kunert [35, 36] defines a coupling function for the deflection of an infinite tooth under single-point loading for cylindrical gears. Spura [37, 38] describes a method for the tooth deflection calculation of gear couplings based on the W/B framework and the coupling function from Kunert. Börner [39] determines the coupling function based on FE results and measurements for cylindrical gears. Schaefer [40] derives the coupling function for bevel gear teeth from FE results. Wu [41] calculates the tooth deflection of skew conical involute gears using a beam model and the coupling function derived by Linke [42]. Linke derives an FE based coupling function in the tooth width direction, so the model could also be considered as a kind of hybrid model. The commercial gear calculation software KISSsoft [43] uses an empirical coupling function, which is validated with FE calculations. Single-slice tooth deflection in KISSsoft is based on the W/B formulation of Petersen [44]. The presented analytical methods have in common that the W/B calculation framework is stand-alone integrated and could easily be exchanged. The W/B method even found its way into international standardization. The equation for tooth stiffness in the ISO 6336 [45] and DIN 3990 [46] is based on a series expansion by Schäfer [47], conducted on the results of calculations using the W/B framework. According to Schäfer [47], the deviation between the series expansion and the mechanical solution is less than 8% [48]. Benkler [49] has developed an analytical tooth deflection method for gear couplings. For the tooth deflection, Benkler solves the differential equation of a bending beam resting on an elastic foundation. The deflection of the gear body itself is adapted from W/B. Furthermore, Benkler calculates the ring gear deflection with a beam model resting on simple hard support bearings at the ends. In contrast to the beam approaches, Kunze [50] superposes different load cases of the planar disk theory to a total solution for the tooth deflection of gear couplings. Due to the available mechanical solutions of a disc, the tooth geometry has to be approximated with a wedge. Theory knowledge of advanced mechanics is necessary to solve the governing elastostatic equations of a disc.

The previous section gives an insight into different common ways of tooth deflection calculation. It is presumptuous that the paper raises completeness over the whole research in the last decades. Therefore, a comprehensive review on analytical, hybrid and numerical methods is given by Marafona et al. in [19]. Natali et al. give a review specially on FE methods for the tooth deflection calculation in [18].

This paper builds on and extends the work of W/B. In the their work, W/B developed the method for the standard basic rack profile [51] and gave the solution for the integrals with graphical nomograms. The approach is valid for steel gears in the plane strain stress state.

In this paper the equations are derived in a closed description for the plane stress and plane strain assumption for any gear tooth geometry and linear material. This makes the equations efficient for implementation in a computerized application and flexible for different gear types. As the teeth are modeled with stub beams, the shear influence on the total deformation increases. This is taken into account with a more detailed calculation of the shear correction factor in this work. Furthermore, the approach is validated with a calculation study. In contrast to validation calculations carried out in most of the literature, the study varies the gear dimensions and point of application force and does not only calculate single mesh configurations.

2 Analytical tooth deflection calculation method

The principle idea for calculating the tooth deflection was published by Weber and Banaschek in 1953 [25]. The method divides the tooth deflection in a bending and a tilting part. The separate parts can be calculated analytically using two substitute models. The tooth-bending mechanism and substitute model is shown in Fig. 1. The mesh force P at a contact point generates the bending deflection w_B around the tooth root. α is the pressure angle at the contact point. Fig. 1b shows the corresponding mechanical model. The tooth gets replaced with a bending beam/truss model. The beam/truss extends from the tooth root radius s r_f to the height y_P where the normal of the contact force crosses the tooth center (line of action). In the ISO 6336 tooth

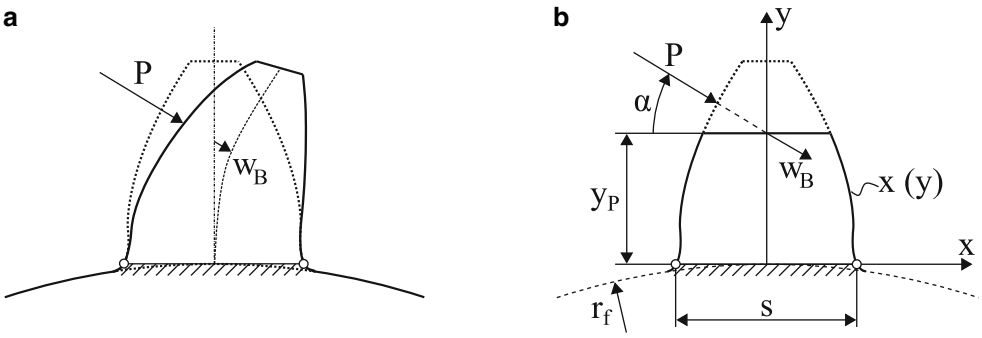

Fig. 1 Tooth bending. **a** Tooth bending around the tooth root, **b** Substitute beam/truss model

root load capacity calculation [52], for example, the tooth is delimited for calculation at the 30° tangent to the gear body. This paper aims to find a general approach which is validated with a FE model. With the definition starting from the dedendum circle, the method is suitable also for special gears and tooth root profiles beside the trochoid root profile. The tooth flank profile can be determined from the standard ISO 21771 [53] or DIN 3960 [54] for an involute gear, while the trochoid tooth root profile calculation method is, among others, specified in [55]. Tooth flank and tooth root form the contour $x(y)$ for the bending beam. The method is not limited to involute gears and can be used for any tooth profile. Since the involute gearing is the industry benchmark for cylindrical gears, the paper uses it as calculation example.

The mesh force P divides into a normal and transverse component:

$$N = P \sin(\alpha), \tag{1}$$

$$Q = P \cos(\alpha). \tag{2}$$

The transverse force induces a moment:

$$M_B = P \cos(\alpha) \left(y_p - y\right). \tag{3}$$

To solve the beam model for the elastic deformation w_B, the deformation work Π_{w_B} equals the strain energy Π_{BB} [56]. The strain energy Π_{BB} consists of a normal (Π_N), shear (Π_Q) and bending part (Π_B):

$$\Pi_{w_B} = \frac{1}{2} P w_B = \Pi_N + \Pi_Q + \Pi_B = \Pi_{BB}. \tag{4}$$

Calculation of the truss strain energy Π_N: The strain energy Π_N of the tooth simplified as a truss gets induced by the normal force N. The stress along the tooth height is

$$\sigma_y = \frac{N}{A} = \frac{P \sin(\alpha)}{2x(y)\, b} \tag{5}$$

and depends on the tooth contour $x(y)$ and the gear facewidth b. To calculate the strain energy, the stress-strain relation is necessary. The described gear model simplifies the 3D volumetric stress-strain state with a 2D plane assumption. Therefore, the plane strain or the plane stress dimension reduction method is suitable. In Fig. 1b, the xy-plane is the reduction plane. For the plane strain assumption, the strain ε_z outside the reduction plane and all z-transverse strains are zero. In contrast, the stress σ_z and the z-transverse stresses are zero for the plane stress assumption. For a linear, isotropic assumption (Hooke's law), usually the modulus of elasticity E and Poisson's ration ν are the descriptive material constants. With the use of the shear modulus

$$G = \frac{E}{2(1+\nu)} \tag{6}$$

and the constant κ, the plane stress and plane strain state can be expressed in one closed formulae framework [57]:

$$\kappa = \begin{cases} 3 - 4\nu, & \text{Plane Strain} \\ \frac{3-\nu}{1+\nu}, & \text{Plane Stress} \end{cases}. \tag{7}$$

Since the cross section stress σ_x is zero for a truss, the stress strain relation simplifies to:

$$\varepsilon_y = \frac{1}{8G} \left[(\kappa + 1)\, \sigma_y + (\kappa + 1) \underbrace{\sigma_x}_{=0} \right] = \frac{(\kappa + 1)\, \sigma_y}{8G}. \tag{8}$$

With the normal force and the stress-strain relation, the strain energy is:

$$\begin{aligned} \Pi_N &= \int_0^{y_p} \frac{1}{2} N \varepsilon_Y \, dy \\ &= \frac{P^2 \sin(\alpha)^2 (\kappa + 1)(1 + \nu)}{8Eb} \int_0^{y_p} \frac{1}{2x(y)} dy. \end{aligned} \tag{9}$$

In the previous equation the shear modulus was replaced by the elastic modulus since this is more known and a tangible material parameter.

Calculation of the shear strain energy Π_Q: The shear strain energy of a beam with the parameters introduced in this paper is:

$$\Pi_Q = \int_0^{y_p} \frac{1}{2}\frac{Q^2}{\chi G A} dy = \frac{P^2 \cos(\alpha)^2}{2\chi G b}\int_0^{y_p} \frac{1}{2x(y)} dy. \quad (10)$$

Weber and Banaschek set $\chi = 5/6$ [25]. In his work, Cowper derives a more detailed calculation for the shear correction factor dependent on the Poisson's ratio [58]. Adapted to the stress-strain relations used in this paper:

$$\chi = \frac{40}{45+\kappa} \quad (11)$$

For $\nu = 0.3$, χ computes to 0.8497 for the plane stress and 0.8547 for the plane strain assumption.

Calculation of the bending strain energy Π_B: The calculation of the internal strain energy is based on the bending beam theory, which is described in detail in the standard literature [59, 60]. The static beam assumption for the stress-strain relations used in this paper is:

$$\sigma_x = \frac{G}{\kappa - 1}\left[(3-\kappa)\varepsilon_y + (\kappa+1)\varepsilon_x\right] = 0. \quad (12)$$

Beam theories assume that the stress σ_x transverse to the tooth height compared to the stress σ_y is small and can be ignored. Equation 12 solved for the strain ε_x gives the correlation to ε_y in the plane stress/plane strain representation. With the previous result and the definition of the shear modulus from Eq. 6, the stress along the beam (tooth height) is:

$$\begin{aligned}\sigma_y &= \frac{G}{\kappa-1}\left[(\kappa+1)\varepsilon_y + (3-\kappa)\varepsilon_x\right] \\ &= \frac{8G}{\kappa+1}\varepsilon_y = \frac{4E}{(\kappa+1)(1+\nu)}\varepsilon_y.\end{aligned} \quad (13)$$

The second beam assumption is that cross sections remain plane after the deformation. Under load, the rotation ψ of a cross section is linear over the tooth thickness and therefore the displacement is [59]:

$$u = \psi x \quad (14)$$

The kinematic equation between the strain and displacement is $((...)' = d(...)/dy)$:

$$\varepsilon_y = \frac{\partial u}{\partial y} = \psi' x \quad (15)$$

With σ_y from Eq. 13, the cutting torque [59] at a specific tooth height evaluates to:

$$M_B = \int \sigma_y x dA = \frac{4EI}{(\kappa+1)(1+\nu)}\psi' \quad (16)$$

I in Eq. 16 is the second moment of inertia for a rectangle. Due to the varying thickness along the tooth height, I also varies:

$$I = \frac{(2x(y))^3 b}{12}. \quad (17)$$

The bending moment from Eqs. 3 and 16 solved for ψ' leads to the internal bending strain energy Π_B in terms of the parameters defined in this paper:

$$\begin{aligned}\Pi_B &= \int_0^{y_p} \frac{1}{2} M_B \psi' dy \\ &= \frac{3(\kappa+1)(1+\nu)}{2Eb}\int_0^{y_p} \frac{{M_B}^2}{(2x(y))^3} dy \\ &= \frac{3P^2\cos(\alpha)^2(\kappa+1)(1+\nu)}{2Eb}\int_0^{y_p} \frac{(y_p - y)^2}{(2x(y))^3} dy.\end{aligned}$$

The summation of the strain energies gives the bending deflection w_B due to the mesh force P:

$$w_B = 2\frac{\Pi_N + \Pi_Q + \Pi_B}{P} \quad (19)$$

The second part of the tooth deflection in the presented theory is the tooth tilting [25]. Fig. 2a shows the deformation schematically. The mesh force P at a contact point generates the tilting deflection w_T around the tooth root. The tooth remains rigid, only the gear body deforms [25]. The mechanic substitute model is shown in Fig. 2b. A half space ($y < 0$) gets loaded with an external constant shear τ_Q and normal σ_N line load. These parts represent the normal and transverse part of the mesh force from Eqs. 1 and 2.

The tilting moment

$$M_T = P\cos(\alpha)\, y_p \quad (20)$$

induced by the transverse force Q is represented by the linear line load σ_B in Fig. 2b. Based on the definition of these simple line loads, it is assumed that the error introduced herein is small due to the integration in calculating the strain energies [25]. The integration balances areas where the simple line load underestimates the actual load against areas where the assumption overestimates the actual load [25]. Furthermore, the place where the stresses act is in some distance to the external loading P, which leads to the conclusion that the type of loading exerts minimal influence on the detailed characteristic of the line load (Saint-Venant

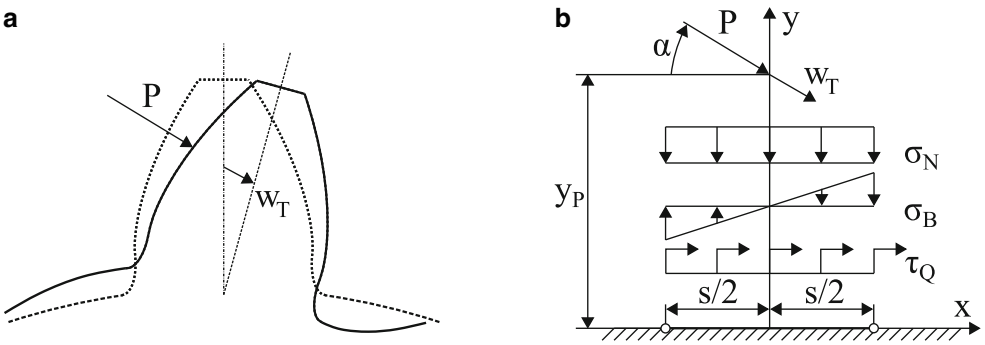

Fig. 2 Tooth tilting. **a** Tooth tilting, **b** Substitute half space model

principle). The load length s is the tooth root thickness at the root radius r_f (see Fig. 1). The approach for calculating the tilting deflection w_T is the same as for the bending deflection. The deformation work of the external load Π_{w_T} equates the strain energy from the line loads:

$$\Pi_{w_T} = \frac{1}{2} P w_T = c_{11} {M_T}^2 + 2 c_{12} M_T Q + c_{22} Q^2 + c_{33} N^2. \quad (21)$$

The factors c are calculated using the complex half-plane approach.

Calculation of c_{11}: The part of the strain energy induced by the external moment M_T gets covered by the linear line load σ_B in Fig. 2b. The deflection is calculated with the complex airy stress function ϕ. The airy stress function ϕ is a harmonic function for solving boundary value problems [61]. With a defined or derived airy stress function, the 2D stresses are [62]:

$$\sigma_x = \frac{\partial \phi}{\partial y} + y \frac{\partial^2 \phi}{\partial^2 y}, \ldots \sigma_y = \frac{\partial \phi}{\partial y} - y \frac{\partial^2 \phi}{\partial^2 y} \quad (22)$$

In the absence of body forces, the airy stress function satisfies the static equilibrium. The stress strain relation for the closed plane stress/plane strain state in y-direction is [57]:

$$\varepsilon_y = \frac{1}{8G} \left[(\kappa - 3) \sigma_x + (\kappa + 1) \sigma_y \right] = \frac{\partial v}{\partial y}. \quad (23)$$

Equation 23 also contains the kinematic relation. Insertion of Eq. 22 and integration for y leads the vertical deflection of the load line 's' in Fig. 2b. G can be replaced with Eq. 6:

$$v_{yR} = \frac{1 + \nu}{E} \left(\frac{\kappa + 1}{2} \phi - y \frac{\partial \phi}{\partial y} \right) \quad (24)$$

Equation 24 still contains the airy stress function ϕ and its derivative. For determining ϕ the line load

$$\sigma_B (u) = \frac{12 M_T}{s^3 b} \quad (25)$$

is assumed [25]. u is the coordinate along the load line. With the general formula [62]

$$\frac{\partial \phi}{\partial y} = \frac{i}{\pi} \int_{a_1}^{a_2} \frac{\sigma_B (u)}{u - z} du. \quad (26)$$

the derivative of the airy stress function ϕ is:

$$\frac{\partial \phi}{\partial y} = -\frac{12 M_T}{s^3 \pi b} \underbrace{Re \left\{ -i z \ln \left(\frac{z - \frac{s}{2}}{z + \frac{s}{2}} \right) - i s \right\}}_{Re\{\cdots\}} \quad (27)$$

Herein $z = x + iy$ is the complex number in cartesian representation. Fig. 3 shows the real part $Re\{\cdots\}$ of Eq. 27 schematically. $Re\{\cdots\}$ equal to πx within the load line and is zero outside. This leads to the internal stresses caused by the load line in Eq. 25 [25].

Integration of Eq. 27 yields the airy stress function

$$\phi = -\frac{12 M_T}{s^3 \pi b} Re \left\{ \frac{1}{2} \left(z^2 - \frac{s^2}{2} \right) \ln \left(\frac{z + \frac{s}{2}}{z - \frac{s}{2}} \right) - \frac{z s}{2} \right\}. \quad (28)$$

for the given loading. With the previous result from Eq. 24

$$v_{yR} = -\frac{(1 + \nu)(\kappa + 1)}{E} \frac{3 M_T}{s^3 \pi b} \cdot \left[\left(x^2 - \frac{s^2}{2} \right) \ln \left(\frac{\left| \frac{s}{2} + x \right|}{\left| \frac{s}{2} - x \right|} \right) - \frac{x s}{2} \right] \quad (29)$$

is the deflection of the half plane at $y = 0$. To calculate the strain energy, Eq. 22 gives the internal stress σ_{yR} at the half plane border ($y = 0$). The integration along the load line yields the stress energy:

$$c_{11} {M_T}^2 = -\frac{1}{2} \int_{-\frac{s}{2}}^{\frac{s}{2}} \sigma_{yR} v_{yR} b dx. \quad (30)$$

Coefficient comparison results in the factor:

$$c_{11} = \frac{9}{4} \frac{(\kappa + 1)(1 + \nu)}{s^2 b E \pi} \quad (31)$$

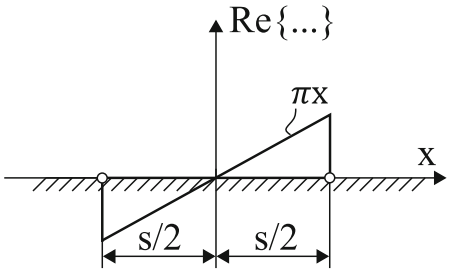

Fig. 3 Real part of the potential function derivative in Eq. 27

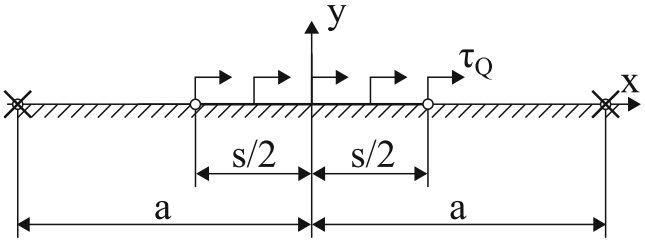

Fig. 4 Boundary condition for determining the deflection due to the external shear load τ_Q

Calculation of c_{12}: The previous factor c_{11} covers the work done by the moment when the load line moves in the negative y-direction (see Fig. 2b). Additionally, with the moment the load line moves in x-direction. This causes work by the transverse force Q, which is covered by the factor c12 in Eq. 21 [25]. The strain in x-direction is [57]:

$$\varepsilon_x = \frac{1}{8G}\left[(\kappa+1)\,\sigma_x + (\kappa-3)\,\sigma_y\right] = \frac{\partial u}{\partial x}. \tag{32}$$

The kinematic relation between ε_x and the displacement u in x-direction is included in Eq. 32. With Eq. 22, it is evident that $\sigma_{yR} = \sigma_{xR}$ at $y = 0$. σ_{xR} is known from the previous c_{11} calculation. Insertion in Eq. 32 and integration yields:

$$u_{xR} = \frac{3\,(\kappa-1)\,(1+\nu)}{E}\frac{M_T}{s^3 b}\left[x^2 - \left(\frac{s}{2}\right)^2\right]. \tag{33}$$

The work performed by the shear line load $\tau_Q = Q/(sb)$ then is:

$$c_{12} M_T\, Q = -\frac{1}{2}\int_{-\frac{s}{2}}^{\frac{s}{2}} \tau_Q u_{yR} b\, dx. \tag{34}$$

Which can be rearranged for the coefficient:

$$c_{12} = \frac{(\kappa-1)\,(1+\nu)}{4Ebs}. \tag{35}$$

Calculation of c_{22}: For the work performed by the transverse force Q, the shear line load $\tau_Q = Q/(sb)$ in Fig. 2b gets applied to the half plane [25]. For a half plane load with an shear line load the stresses are [63]:

$$\sigma_x = -2\frac{\partial\phi}{\partial y} - y\frac{\partial^2\phi}{\partial x\partial y}, \sigma_y = y\frac{\partial^2\phi}{\partial x\partial y},\ \tau_{xy} = -\frac{\partial\phi}{\partial y} - \frac{\partial^2\phi}{\partial^2 y} \tag{36}$$

Herein ϕ is again a complex airy stress function. τ_Q in Eq. 26 instead of σ_B yields the derivative of ϕ:

$$\frac{\partial\phi}{\partial y} = \frac{Q}{sb\pi} Re\left\{ i \ln\left(\frac{z-\frac{s}{2}}{z+\frac{s}{2}}\right)\right\} \tag{37}$$

Integration gives:

$$\phi = \frac{Q}{sb\pi} Re \left\{\left(z-\frac{s}{2}\right)\ln\left(z-\frac{s}{2}\right) - \left(z+\frac{s}{2}\right)\ln\left(z+\frac{s}{2}\right)\right\}. \tag{38}$$

With the kinematic relation from Eq. 32 and the stresses from Eq. 36, integration for x results in the displacement of the load line:

$$u_{xR} = \frac{(\kappa+1)\,(1+\nu)\,Q}{sbE\pi} \left[\left(x+\frac{s}{2}\right)\ln\left|x+\frac{s}{2}\right| - \left(x-\frac{s}{2}\right)\ln\left|x-\frac{s}{2}\right|\right] \tag{39}$$

at the boundary $y = 0$ of the half plane. With the use of the complete half plane determining the strain energy, the displacements would be infinite [25]. Therefore, the half plane has to be clamped at a reasonable distance [25]. This boundary condition is depicted with crosses in Fig. 4. The half plane gets fixed at the horizontal distance 'a' from the middle of the tooth at $x = 0$.

A point $|x| = a > s/2$ outside the load line moves by:

$$u_{aR} = \frac{(\kappa+1)\,(1+\nu)\,Q}{sbE\pi} \left[\left(a+\frac{s}{2}\right)\ln\left(a+\frac{s}{2}\right) - \left(a-\frac{s}{2}\right)\ln\left(a-\frac{s}{2}\right)\right]. \tag{40}$$

The described boundary condition yields a movement of $u_Q = u_{aR} - u_{xR}$ at the boundary of the load line. The stress energy for the shear load case is:

$$c_{22} Q^2 = -\frac{1}{2}\int_{-\frac{s}{2}}^{\frac{s}{2}} u_Q \tau_Q b\, dx \tag{41}$$

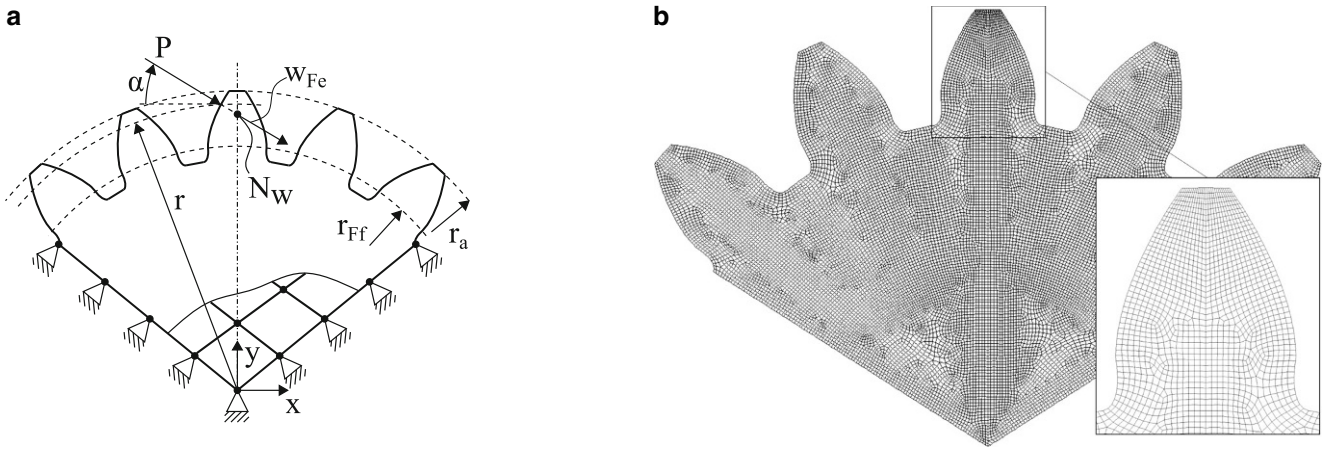

Fig. 5 Finite element tooth deflection calculation model. **a** BC's and deformation result determination, **b** Finite element meshing

This, upon integration and coefficient comparison, leads to the factor

$$c_{22}\left(\frac{a}{s}\right) = \frac{(\kappa+1)(1+\nu)}{4bE\pi} \left[\left(\frac{a}{s}+\frac{1}{2}\right)\ln\left(\frac{a}{s}+\frac{1}{2}\right) - \left(\frac{a}{s}-\frac{1}{2}\right)\ln\left(\frac{a}{s}-\frac{1}{2}\right)+\frac{1}{2}\right] \tag{42}$$

dependent on the ratio a/s. The ratio puts the boundary distance in proportion to the tooth ground thickness. For the final determination of c_{22}, the mean value for $a/s = 2$ and $a/s = 3$ is proposed, which corresponds to the second-nearest tooth [25]:

$$c_{22} = \frac{c_{22}(2) + c_{22}(3)}{2} \tag{43}$$

Calculation of c_{33}: The factor c_{33} covers the stress energy induced by the normal part of the mesh force with σ_N in Fig. 2b. In the calculation of c_{22}, the half plane has to be fixed to avoid infinite displacements. The same problem is encountered when calculating c_{33}. Therefore, Weber and Banaschek propose estimating the factor with the ratio of the strain energy Π_N and Π_Q as based on the determination of the tooth bending [25]:

$$\frac{\Pi_N}{\Pi_Q} = \frac{c_{33}N^2}{c_{22}Q^2} \tag{44}$$

The assumption is that the strain energies between the tooth bending and gear body deflection behave similarly [25]. With these comparative assumption, the factor c_{33} calculates to:

$$c_{33} = \frac{\chi(\kappa+1)}{8}c_{22} \tag{45}$$

With the calculation of the c-factors, the tooth tilting deformation w_T follows from Eq. 19:

$$w_T = 2\frac{c_{11}M_T{}^2 + 2c_{12}M_T Q + c_{22}Q^2 + c_{33}N^2}{P}. \tag{46}$$

The total analytical tooth deformation w_A is the sum of the tooth tilting part w_T and tooth bending part w_B from Eq. 19. This approach allows to add a third part based on any contact stiffness formulation to determine the overall tooth deformation.

3 Finite element tooth-deflection calculation model

In this section, a linear finite element (FE) model is described in theory with the external loads and boundary conditions for the comparative calculations. Ansys mechanical APDL R1 [64] is used for the model creation and solution. Fig. 5a shows the structure and the boundary conditions of the gear segment model. As with the analytical theory, the FE model is also plane (2D). The involute tooth geometry is taken from the previous section. The tooth, for which the deformation is calculated, lies symmetrically to the y-axis. To cover the stiffening effect of the teeth right and left to the loaded tooth, two extra teeth are modeled on each side. This coincides with the presented analytical theory. The gear body segment extends from the tooth ground to the gear center as shown in Fig. 5a. The geometry gets meshed with PLANE183 Elements from the Ansys library [64], which have quadratic shape functions. Fig. 5b shows the convergent mesh exemplary. The main and relevant parts, where the loading applies and the deformation is measured, are mapped meshed with eight-node quadrilaterals. Some transition zones are meshed with 6-node triangles

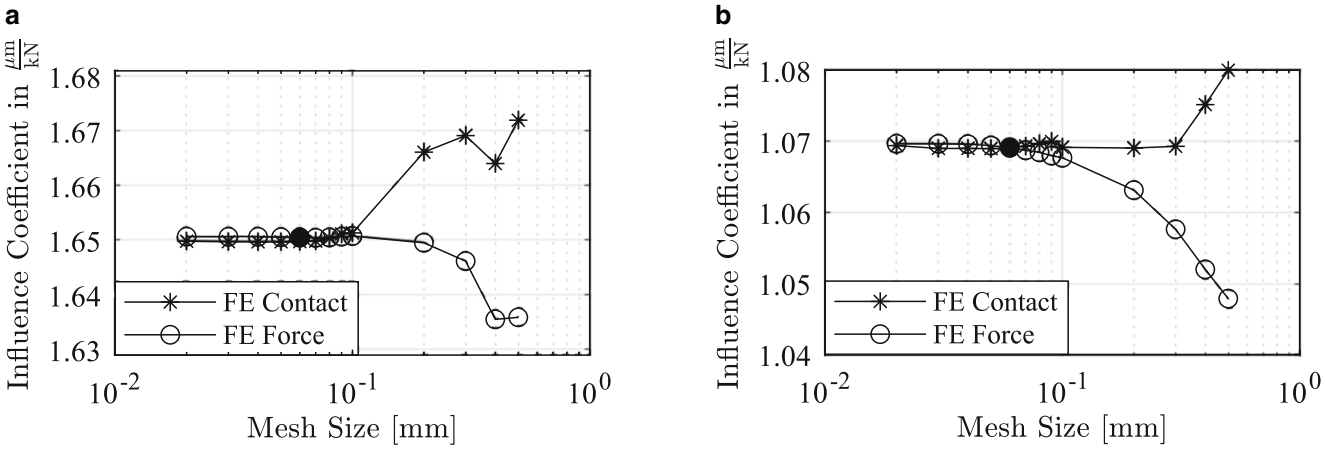

Fig. 6 Finite element convergence analysis with the linear and contact model. **a** 15 teeth, **b** 100 teeth

to make the mesh transition between the complex geometry elements. The external point force P is applied at a radius r normal to the involute flank profile between the dedendum form circle r_{Ff} and the addendum circle r_a. Fig. 5a shows symbolically the Dirichlet boundary conditions applied to the sides of the gear body. All degrees of freedom are fixed at these nodes.

With the analytical model, the tooth deflection is calculated in the direction of the external load, which is the direction of the line of action. Similarly, w_{Fe} is the tooth deflection from the FE calculation as shown in Fig. 5a. The deformation w_{Fe} of the FE calculation is determined at the node N_w, which is located at the point y_p of the analytical model (see Fig. 1b). w_{Fe} is divided by the external force P, which yields the influence coefficient (IC):

$$q_{FE} = \frac{w_{FE}}{P}. \tag{47}$$

The teeth number significantly influences the dimensions of the gear. Hence, the teeth number is varied from 15 to 100 in the following calculation study. Table 1 contains the gear parameters used for the analysis. The extremal teeth values 15 and 100 were used for the convergence analysis of the FE model. However, the FE model is built with five teeth for every analysis step as shown in Fig. 5. Additionally, the loading with a single point force is investigated to exclude negative effects on the calculated displacement. Therefore, a nonlinear FE contact model, similar to the described one from Fig. 5a, is used. In contrast to the point loading, the load is applied on a rigid cylinder that contacts the gear tooth at the force application point. The radius of the cylinder corresponds to the curvature radius of an equal mating gear at the contact point. For both models, the load respectively the contacting cylinder is applied at the mean radius between the addendum circle and dedendum form circle. Fig. 6 shows the results from the convergence analysis, in which the default edge length of the elements was incrementally reduced from 0.5 mm to 0.02 mm. In Fig. 6a, the model with 15 teeth is shown, while Fig. 6b shows the model with 100 teeth. The line with the circle markers is the deflection for the single point loading over different mesh sizes. The line with the asterisk markers is the deflection for the contact model. It is obvious that both models converge for decreasing mesh size. In the convergent area from mesh size 0.06 mm to 0.02 mm the maximum relative error between the force and contact model is 0.06% for both 15 and 100 teeth. For the comparative calculations in the next chapter, a mesh size of 0.06 mm and the linear FE model is used (black-filled circle marker in Fig. 6).

4 Comparative calculations

In this section, the results from the presented analytical tooth deflection calculation method are compared to the FE Model. Table 1 shows the basic gear parameters used for the analysis.

To investigate the influence of the gear size, the teeth number is varied incrementally from 15 to 100. The teeth number is increased by one in each calculation. Fig. 7a shows the gear transverse section for the smallest (15 teeth) and largest (100 teeth) size variant. Furthermore, the influence of the point of application force is investigated. Eleven force positions along the tooth profile direction are exam-

Table 1 Characteristic gear parameters used for the comparative calculations. Names according DIN 3960 [54]

Normal module m_n [mm]	Profile shift coefficient x [–]	Normal pressure angle α_n [°]	Addendum factor h_a^* [–]	Dedendum factor h_f^* [–]	Teeth number range z [–]
1	0.3	20	1.0	1.25	[15, ... 100]

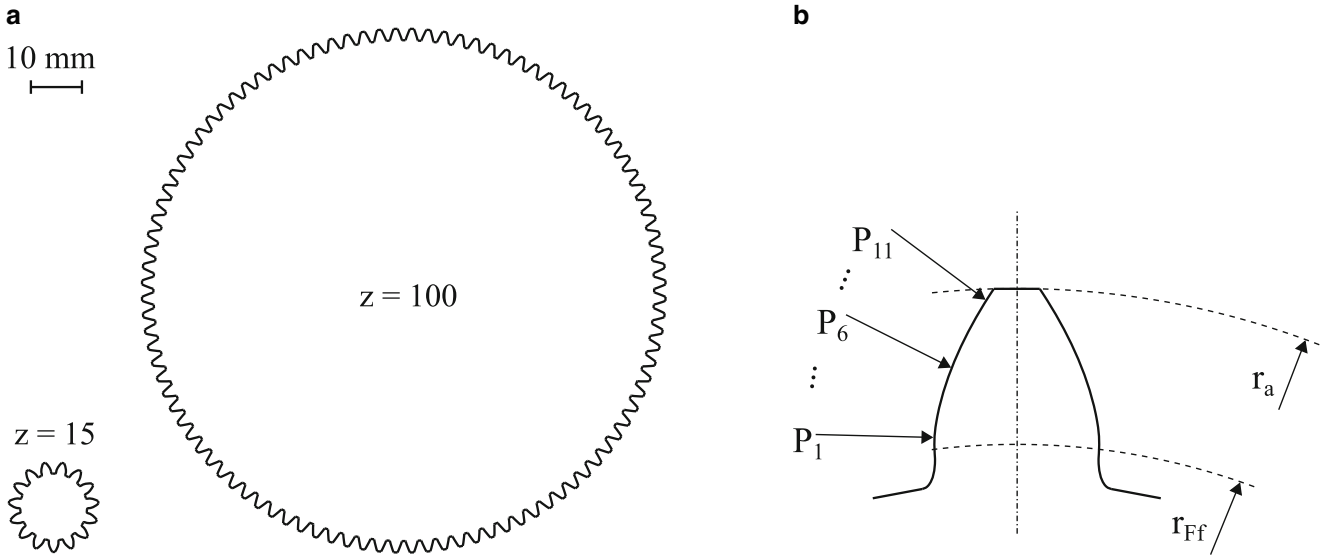

Fig. 7 Variation in the calculation study. **a** Smallest and largest size (teeth number), **b** Points of application force

ined at each model. The positions are equally spaced between the dedendum form circle r_{Ff} and addendum circle r_a with 5% indent of the involute tooth depth at each limiting radius as shown in Fig. 7b. Eleven radii at 86 different models (teeth numbers) lead to 946 single FE and analytical calculations.

The influence coefficient for the analytical calculation follows from the exchange of the deflection w in Eq. 47. The relative deviation between the FE and analytical influence coefficient in percent is:

$$\triangle = \frac{q_A - q_{FE}}{q_{FE}} * 100. \tag{48}$$

Fig. 8 shows the 946 deviations from the calculation study between the analytical and FE calculation. In Fig. 8a, the deviations are grouped in bins, sorted and displayed as a histogram. The vertical axis in Fig. 8a gives the quantity in each bin. The horizontal axis in Fig. 8a shows the deviation in percent from Eq. 48. Two extreme deviation bins are obvious. One bin with 79 single deviations around 2% and another bin with 81 around 9.2%. The overall minimum deviation is –11.42%, the overall maximum deviation is 10.05%. Fig. 8b shows the deviations over the involute tooth depth evaluated and sorted for all size variants. Each Boxplot in Fig. 8b represents one point of application force and contains the deviations from the 86 size variants. 5% on the horizontal axis in Fig. 8b corresponds to the force

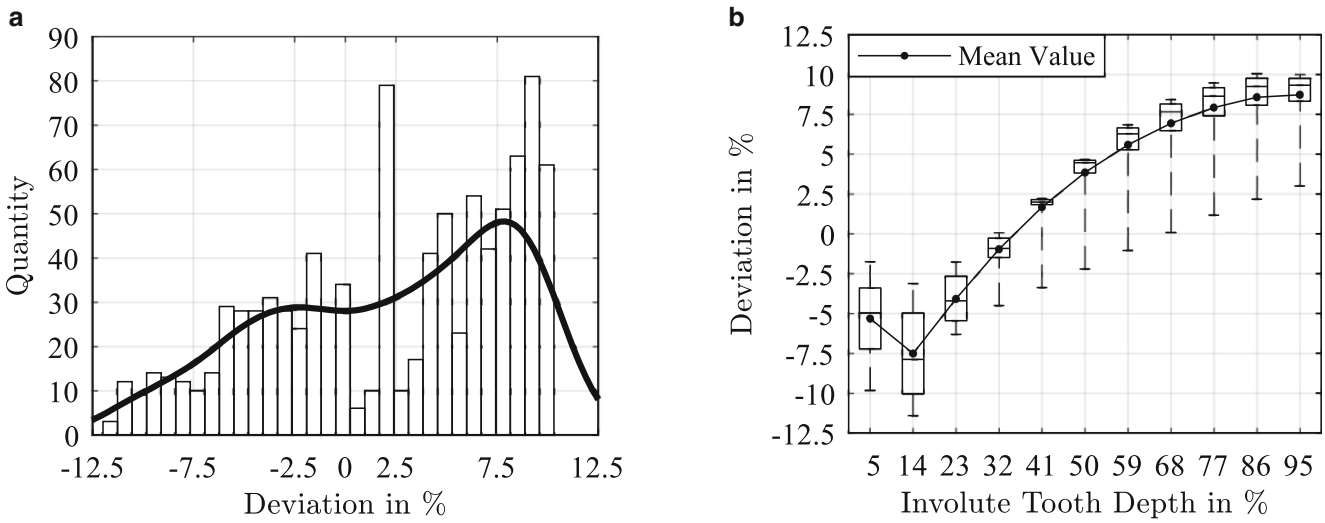

Fig. 8 Deviations between the finite element model and the presented analytical method. **a** All deviations sorted as Histogram (sum equals to 946), **b** Boxplot analysis for the different sizes at the eleven discrete radii (*horizontal axis*)

vector P_1 in Fig. 7b. The remaining points are sorted in ascending order along the tooth height till the force vector P_{11} at 95% of the involute tooth depth. The boxplot whiskers extend to the minimum/maximum of each data set. The solid horizontal line in the boxes represents the median. The line plot with black-filled circle markers in Fig. 8b shows the mean values. Since the deviations are negative up to 32% involute tooth depth, the analytical deflection is lower than the FE deflection. From 41% to 68% involute tooth depth, the interquartile range of each box includes only positive deviations. Hence, more than 50% of the FE deflections are lower than the analytical deflections in this range. From 68% involute tooth depth, all deviations are positive and therefore the FE deflection always lower than the analytical deflection. From 14% involute tooth depth, the boxplot analysis shows a clear and steady progression of the deviation.

Below 14% involute tooth depth, the deviations do not follow the trend in Fig. 8b. The absolute mean deviation between the FE model and the analytical deviation is lower at 5% involute tooth depth. The difference between the mean values at 5% and 14% involute tooth depth is 2.2%. The analytical calculation method projects the force vector onto the middle plane of the tooth (distance y_p in Fig. 1b and 2b). For the point of application force at 5% involute tooth depth (P_1 in Fig. 7b) and the size variants with $z \geq 49$ the projection extends into the gear body. This is shown schematically in Fig. 9a. The distance y_p is negative and the force vector extends below the root radius r_f. Fig. 9b shows the value of y_p for the different size variants. y_p is negative from $z \geq 49$. For configurations with this behavior the analytical model assumes that the tooth bending w_B deflection is zero. The tooth tilting deflection w_T from Eq. 46 calculates with the negative value y_p. The discontinuous trend in Fig. 8b becomes clear when looking at the deviation for different size variants.

Fig. 10 shows the results for four single size variants. Subplot Fig. 10a contains the results for 15 teeth, Fig. 10b for 49 teeth, Fig. 10c for 60 teeth and Fig. 10d for 100 teeth. As in Fig. 8b, the horizontal axes of the subplots indicates the involute tooth depth. The vertical axis on the left side of each subplot specify the influence coefficients with the triangle markers for the FE and the circle markers for the analytical calculation. The vertical axis on the right side of each subplot specify the deviation between both methods, which is noted herein with asterisk markers. For the size variant with $z = 49$, y_p is $-1.28\,\mu m$ and the deviation progression in Fig. 10b is steady. With $z = 60$, y_p becomes $-56.43\,\mu m$. For this size variant the deviation progression in Fig. 10c shows a clear discontinuity. For the largest size variant with $z = 100$, y_p is $-159.05\,\mu m$ and therefore Fig. 10d shows a significant discontinuity. The discontinuity correlates with the value of y_p.

Fig. 10 shows that the analytical and FE influence coefficients curves have a similar shape. The influence coefficient/deflection increases in the tooth height direction and, as seen in the boxplot analysis, the deviation changes from negative to positive. Additionally, the spread between the minimum and maximum deviation becomes larger over the size variants. The spread increase from 15 teeth to 49 teeth is considerably larger than the spread increase from 60 teeth to 100 teeth.

5 Discussion of the validation

The comparison between the analytical and FE deformation calculation from the previous section shows a good correlation. The expectation that the tooth deflection increases from the tooth root to the tooth tip is confirmed. Both calculation methods show the same trend and the result graphs are similar in shape. From the point of view of the authors, the spread in the deviation from –11.42% to 10.05% is acceptable, especially when keeping in mind, that even the standards ISO 6336 [45] and DIN 3990 [46] accept a deviation of 8 % in their series development of the tooth deflection calculation [48].

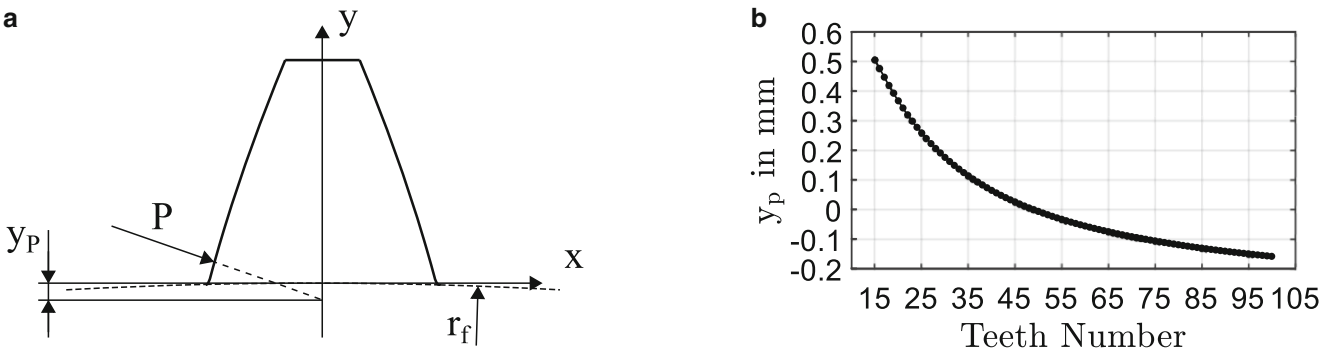

Fig. 9 Projection of the point of application force onto the middle plane of the tooth. **a** Projected point for application force near the tooth root, **b** Value of y_p over the teeth number

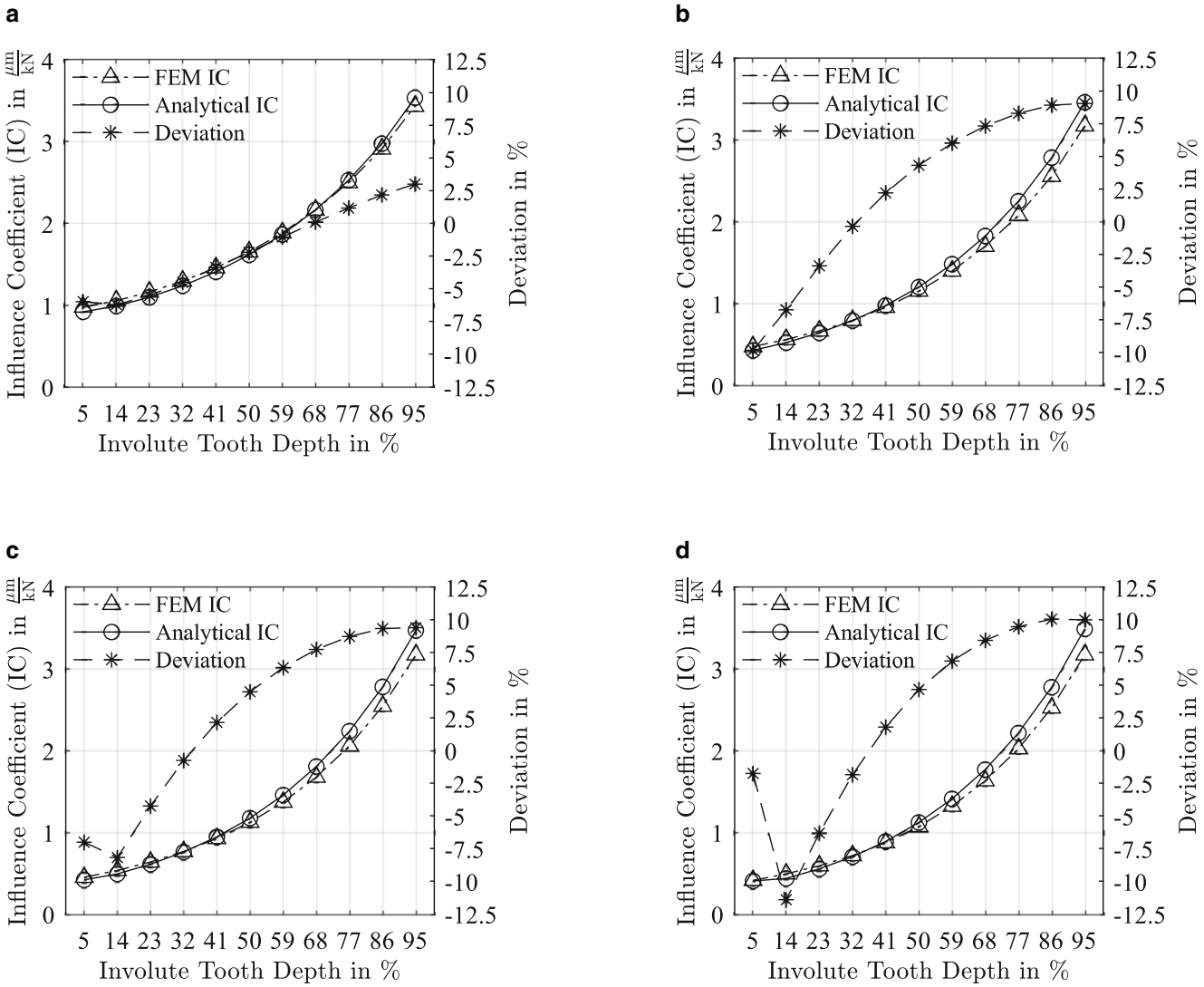

Fig. 10 Deviation between the analytical and FE tooth deflection calculation for different size variants. **a** 15 teeth, **b** 49 teeth, **c** 60 teeth, **d** 100 teeth

From the results in Fig. 8b, it is obvious that the deviation between the analytical and FE model changes from negative to positive over the tooth height. In the meshing of two gears, the teeth flanks come in contact with each other in opposite directions. This means that the tooth tip contacts the mating gear in the tooth root area. The over- and underdetermination of the tooth deflection is thus at least partially canceled out. The authors understand that this is an engineering point of view. But this allows the assumption that the total deformation in the teeth meshing tends to be better estimated and errors do not accumulate.

Fig. 10a–d shows that the minimum and maximum deviation increases with an increasing teeth number. Since the change in the deviation becomes smaller with an increasing teeth number, it can be assumed that the minimum and maximum deviation do not increase considerably further for teeth number $z > 100$. The deviations show an asymptotic behavior.

The deviation graphs in Fig. 8b and 10c, d shows a discontinuity between 5% and 23% involute tooth depth, which is explained with the projection of the point of application force into the gear body. For 5% involute tooth depth, the deviation between the analytical and FE model is better than for 14%. A point of application force near the tooth root (e.g., 14% involute tooth depth) violates the validity of the analytical substitute models. The length y_p of the beam model is extremely low. Beams are long prismatic structures where one dimension is recently larger than the others [60]. Furthermore, the simplified external loads on the half plane model in Fig. 2b are based on the assumption that the point of application force is sufficiently distant (Saint-Venant principle). Strictly speaking, both assumptions are not fulfilled near the tooth root. For example, y_p

is 38.54 μm for $z = 100$ at 14% involute tooth depth. For the deflection calculation at 5% involute tooth depth and $z \geq 49$, the beam deflection is zero and the value of y_p is used with the negative sign for the half plane deflection. Based on the results in Fig. 10b–d, this assumption seems to be justified since the deviation is better at a 5% involute tooth depth.

Gearings with a normal module of 1 mm are subject of the comparative calculation. The research by Braykoff [65] concludes that the meshing stiffness is independent of the size and depends on the material characteristics and the geometry itself. This leads to the conclusion that the results presented in this paper are transferable to gearings with other normal modules.

Further studies on the experimental and simulative validation of the analytical tooth deflection calculation method can be found in the literature. Winter and Podlesnik [66–68] perform tooth deformation measurements on gears in a pulsator test rig. The measured tooth deflection of gears with a solid body is in good agreement with the calculation results from the W/B method [25]. Winter and Podlesnik suggest a correction factor to compensate for the decreasing tooth stiffness for wheel bodies with webs and/or thin rims.

The load distribution in a gear stage is directly related to the tooth deflection. Daffner [69, 70] measures the load distribution of gears with different body geometries and compares it with the results from the gear calculation software RIKOR [71]. RIKOR calculates the tooth deflection according to the W/B approach [72]. While the experimental and simulative line load shows a good agreement for the solid gear body, significant large deviations are observable for gear bodies with (asymmetrical) webs. Based on FE calculations, Daffner [69] proposes a correction function for gear geometries with asymmetrical webs.

Geiser and Schinagl [73] measure the tooth deflection in a pulsator test rig. To determine the deformation of the pulsator clamping, a cylinder with a gear equivalent radius of curvature is also measured. The deformation calculation of a cylinder is validated. This allows the deformation of pulsator clamping to separate from the deformation of the test specimen. In addition to the experiments, Geiser and Schinagl calculate the tooth deflection with the analytical W/B and FE the method. Depending on the applied load, the deviation between the calculated and measured values varies from 6% to 11%, where the measured deformations are consistently larger than the calculated ones.

6 Conclusion

In this paper, an analytical method for the tooth deflection calculation has been presented. The mathematical framework is based on the work by Weber and Banaschek [25] and was derived with the common constitutive equations for the plane stress and plane strain state. The presented description simplifies the implementation for applications where both states are of interest. Materials other than steel can be specified. Furthermore, the influence of the boundary condition for the half plane in the tooth tilting calculation can be investigated with the derived general formula of the factor c_{22} in Eq. 43. This is especially helpful in applications with alternative gear body geometries (e.g., for face gears). The shear influence is considered more precisely by a detailed calculation of the shear correction factor. In contrast to numerical approaches, the analytical method is fast and free of discretization errors. For the simulative validation, a linear FE model for the tooth deflection calculation is introduced. In a convergence analysis, the model shows its validity and equality with a contact model.

The simulative validation in this paper supplemented by investigations from the literature shows that the analytical method is a good starting point for calculating gear tooth deflection with a standard gear body geometry. Further investigations could focus on complex gear body geometries. It is assumed that the half plane approach is insufficient for gears with thin rims (e.g., planetary gears). Depending on the design of the gear body, the stiffness itself can vary. For gear designs where the body is wider than the tooth face width, an additional supporting effect can be expected. This cannot be captured by the current half plane model. In particular, gears with a low number of teeth (pinions) are often manufactured directly onto the shaft. In this case, the transverse sections at the tooth face sides are directly connected to the shaft. The beam substitute model cannot capture this additional supporting effect. It can be seen that the analytical tooth stiffness calculation is far from being

Table 2 Nomenclature

P	Mesh force	N	Normal force
Q	Transverse force	α	Pressure angle
M_B	Bending moment	y_p	Point of application force
w_B	Tooth bending deflection	b	Gear face width
$x\,(y)$	Tooth contour	E	Modulus of elasticity
ν	Poisson's ration	G	Shear modulus
κ	Plane stress/strain constant	I	Geometrical moment of inertia
w_T	Tooth tilting deflection	M_T	Tilting Moment
ϕ	Complex airy stress function	s	Tooth thickness at the root radius
a	Distance for the boundary condition	w_A	Analytical tooth deflection
w_{FE}	Numerical tooth deflection	q_{FE}	Tooth compliance
$\triangle$	Deviation		

fully explored. The authors hope that the paper is a good starting point for further research.

7 Nomenclature

The nomenclature is shown in Table 2

Funding Open Access funding enabled and organized by Projekt DEAL.

Conflict of interest J.-F. Hochrein, M. Otto and K. Stahl declare that they have no competing interests.

References

1. Otto M, Fromberger M, Stahl K (2017) Gear mesh resonance and stiffness validated in calculation and experiment. 24th International Congress on Sound and Vibration, ICSV, pp 2930–2937
2. Kohn B, Utakapan T, Fromberger M et al (2017) Flank modifications for optimal excitation behaviour. Forsch Ingenieurwes 81:65–71. https://doi.org/10.1007/s10010-017-0218-0
3. Bong HB (1990) Erweiterte Verfahren zur Berechnung von Stirnradgetrieben auf der Basis numerischer Simulationen und der Methode finiter Elemente. Dissertation, Rheinisch-Westfälische Technische Hochschule Aachen
4. Neupert B (1982) Berechnung der Zahnkräfte, Pressungen und Spannungen von Stirn- und Kegelradgetrieben. Dissertation, Rheinisch-Westfälische Technische Hochschule Aachen
5. Neupert B (1983) Berechnung der Zahnkräfte, Pressungen und Spannungen von Stirn- und Kegelradgetrieben. Fortschrittberichte der VDI Zeitschriften 125:360–361
6. Schäfer J (2008) Erweiterung des Linienkontaktmodells für die Finite Elemente-basierte Zahnkontaktanalyse von Stirnradverzahnungen. Dissertation, Rheinisch-Westfälische Technische Hochschule Aachen
7. Schäfer J, Schlattmeier H, Weck M (2003) FVA-Nr. 377 – Heft 723 – Kontaktmodell mehrfacher Zahneingriff: Berechnung von Stirnradpaarungen mit Mehrfacheingriffen mit Hilfe der Finite-Elemente-Methode. Forschungsvereinigung Antriebstechnik e. V., Frankfurt/Main
8. Vijayakar S (1991) A combined surface integral and finite element solution for a three-dimensional contact problem. Int J Numer Meth Engng 31:525–545. https://doi.org/10.1002/nme.1620310308
9. Vijayakar SM, Busby HR, Houser DR (1987) Finite element analysis of quasi-prismatic bodies using Chebyshev polynomials. Int J Numer Meth Engng 24:1461–1477. https://doi.org/10.1002/nme.1620240805
10. Vijayakar SM, Busby HR, Houser DR (1988) Linearization of multibody frictional contact problems. Computers & Structures 29:569–576. https://doi.org/10.1016/0045-7949(88)90366-5
11. Boussinesq J (1885) Application des potentiels a l'etude de l'equilibre et du movement des solides elastique. Gauthiers-Villar, Paris
12. Guingand M, de Vaujany J-P, Jacquin C-Y (2005) Quasi-static analysis of a face gear under torque. Comput Methods Appl Mech Eng 194:4301–4318. https://doi.org/10.1016/j.cma.2004.10.010
13. Vedmar L (1981) On the Design of External Involute Helical Gears. Division of Machine Elements, Department of Mechanical Engineering, Lund Institute of Technology., Lund
14. Chang L, Liu G, Wu L (2015) A robust model for determining the mesh stiffness of cylindrical gears. Mech Mach Theory 87:93–114. https://doi.org/10.1016/j.mechmachtheory.2014.11.019
15. Feng S, Chang L, He Z (2020) A hybrid finite element and analytical model for determining the mesh stiffness of internal gear pairs. J Mech Sci Technol 34:2477–2485. https://doi.org/10.1007/s12206-020-0523-7
16. Beinstingel A, Keller M, Heider M et al (2021) A hybrid analytical-numerical method based on Isogeometric Analysis for determination of time varying gear mesh stiffness. Mech Mach Theory 160:104291. https://doi.org/10.1016/j.mechmachtheory.2021.104291
17. Beinstingel A, Heider M, Pinnekamp B et al (2021) Gear mesh excitation and non-uniform Rational B-Splines. Forsch Ingenieurwes. https://doi.org/10.1007/s10010-021-00524-4
18. Natali C, Battarra M, Dalpiaz G et al (2021) A critical review on FE-based methods for mesh stiffness estimation in spur gears. Mech Mach Theory. https://doi.org/10.1016/j.mechmachtheory.2021.104319
19. Marafona JD, Marques PM, Martins RC et al (2021) Mesh stiffness models for cylindrical gears: A detailed review. Mech Mach Theory. https://doi.org/10.1016/j.mechmachtheory.2021.104472
20. Hong J, Talbot D, Kahraman A (2014) A semi-analytical load distribution model for side-fit involute splines. Mech Mach Theory 76:39–55. https://doi.org/10.1016/j.mechmachtheory.2014.02.002
21. Yau E, Busby HR, Houser DR (1994) A rayleigh-ritz approach to modeling bending and shear deflections of gear teeth. Computers & Structures 50:705–713. https://doi.org/10.1016/0045-7949(94)90429-4
22. Stegemiller ME, Houser DR (1993) A Three-Dimensional Analysis of the Base Flexibility of Gear Teeth. J Mech Des 115:186–192. https://doi.org/10.1115/1.2919317
23. Del Fernandez Rincon A, Viadero F, Iglesias M et al (2013) A model for the study of meshing stiffness in spur gear transmissions. Mech Mach Theory 61:30–58. https://doi.org/10.1016/j.mechmachtheory.2012.10.008
24. Iglesias M, Del Fernandez Rincon A, de-Juan A et al (2015) Advanced model for the calculation of meshing forces in spur gear planetary transmissions. Meccanica 50:1869–1894. https://doi.org/10.1007/s11012-015-0130-3
25. Weber C, Banaschek K (1953) Formänderung und Profilrücknahme bei gerad- und schrägverzahnten Rädern. Schriftreihe Antriebstechnik vol 11. Vieweg-Verlag, Braunschweig
26. Lewis W (1892) Investigation of the strength of gear teeth. Proc. of the Engineers Club November / December, pp 19–23
27. Schmidt G (1972) Berechnung der Wälzpressung schrägverzahnter Stirnräder unter Berücksichtigung der Lastverteilung. Dissertation, Technische Universität München
28. Placzek T (1988) Lastverteilung und Flankenkorrektur in gerad- und schrägverzahnten Stirnradstufen. Dissertation, Technische Universität München
29. Wikidal F (1998) Berechnung der Flankenpressung gerad- und schrägverzahnter Stirnräder unter Berücksichtigung last- und fertigungsbedingter Abweichungen. Dissertation, Technische Universität München
30. Otto M (2009) Lastverteilung und Zahnradtragfähigkeit von schrägverzahnten Stirnrädern. Dissertation, Technische Universität München

31. Utakapan T (2020) Schwingungsverhalten mehrstufiger Getriebe. Dissertation, Technische Universität München
32. Conry TF, Seireg A (1971) A Mathematical Programming Method for Design of Elastic Bodies in Contact. J Appl Mech 38:387–392. https://doi.org/10.1115/1.3408787
33. Conry TF, Seireg A (1973) A Mathematical Programming Technique for the Evaluation of Load Distribution and Optimal Modifications for Gear Systems. J Eng Ind 95:1115–1122. https://doi.org/10.1115/1.3438259
34. Lutz M (2000) Methoden zur rechnerischen Ermittlung und Optimierung von Tragbildern von Schneckengetrieben. Dissertation, Technische Universität München
35. Kunert J, Trempler U, Wikidal F (1995) FVA-Nr. 224/I+II – Heft 458 – Lastverteilungsmessung: Weiterentwicklung der Grundlagen zur Ermittlung der Lastaufteilung und Lastverteilung bei außenverzahnten Gerad- und Schrägstirnrädern durch Verformungs- und Spannungsmessungen. Forschungsvereinigung Antriebstechnik e.V., Frankfurt/Main
36. Kunert J (1999) Experimentell gestützte Untersuchungen zum Verformungs- und Spannungsverhalten an außenverzahnten Stirnrädern für eine verbesserte Beanspruchungsanalyse. Dissertation, Technische Universität Dresden
37. Spura C, Berger G (2011) Ermittlung des Verformungs- und Steifigkeitsverhaltens von bombierten Profilwellenverbindungen mit Evolventenverzahnung. Forsch Ingenieurwes 75:35–44. https://doi.org/10.1007/s10010-011-0132-9
38. Spura C (2015) Berechnung der Verformungen und Steifigkeiten evolventischer Verzahnungen von Zahnkupplungen. Forsch Ingenieurwes 79:5–15. https://doi.org/10.1007/s10010-015-0183-4
39. Börner J, Kurz N, Joachim F (2002) Effective analysis of gears with the program LVR. Verein Deutscher Ingenieure: International Conference on Gears, Garching bei München. VDI-Bericht 1665:721–733
40. Schaefer S (2017) Verformungen und Spannungen von Kegelradverzahnungen effizient berechnet. Dissertation, Technische Universität Dresden
41. Wu S-H, Tsai S-J (2009) Contact stress analysis of skew conical involute gear drives in approximate line contact. Mech Mach Theory 44:1658–1676. https://doi.org/10.1016/j.mechmachtheory.2009.01.010
42. Linke H, Börner J (1996) Stirnradverzahnung: Berechnung, Werkstoffe, Fertigung. Hanser, München
43. KISSsoft AG—A Gleason Company (ed) (2019) KISSsoft Release 2019: Benutzerhandbuch
44. Petersen D (1989) Auswirkungen der Lastverteilung auf die Zahnfußtragfähigkeit von hoch überdeckenden Stirnradpaarungen. Dissertation, Technische Universität Braunschweig
45. ISO 6336-1:2019-11 (2019) Calculation of load capacity of spur and helical gears—Part 1: Basic principles, introduction and general influence factors
46. DIN 3990-1:1987–12 (1987) Tragfähigkeitsberechnung von Stirnrädern – Einführung und allgemeine Einflußfaktoren
47. Schäfer S (1971) Ein Beitrag zur Ermittlung des wirksamen Flankenrichtungsfehlers bei Stirnradgetrieben und der Lastverteilung bei Geradverzahnung. Dissertation, Technische Hochschule Darmstadt
48. Otto M, Fromberger M, Stahl K (2016) Die Verzahnungssteifigkeit in Berechnung und Experiment. SMK – Schweizer Maschinenelemente Kolloquium, pp 33–44
49. Benkler H (1969) Der Mechanismus der Lastverteilung an bogenverzahnten Zahnkupplungen. Dissertation, Technische Hochschule Darmstadt
50. Kunze G (1988) Untersuchungen zur Beurteilung von Verzahnungen für Mitnehmerverbindungen, insbesondere von Zahnkupplungen. Habilitation, Technische Universität Dresden
51. British Standard Institution (1940) BS 436, Specification for machine cut gears: A. helical and straight spur, London
52. ISO 6336-3:2019-11 (2019) Calculation of load capacity of spur and helical gears—Part 3: Calculation of tooth bending strength
53. DIN ISO 21771:2014-08 (2014) Zahnräder – Zylinderräder und Zylinderradpaare mit Evolventenverzahnung – Begriffe und Geometrie
54. DIN 3960:1987-03 (1987) Begriffe und Bestimmungsgrößen für Stirnräder (Zylinderräder) und Stirnradpaare (Zylinderradpaare) mit Evolventenverzahnung
55. Linke H, Börner J, Heß R (eds) (2016) Cylindrical gears: Calculation—materials—manufacturing, 1st edn. Hanser, Munich
56. Weber C (1947) Festigkeitslehre. Bücher der Technik (Notdruck). Wolfenbütteler Verlags Anstalt, Wolfenbüttel-Hannover
57. Kienzler R, Schröder R (2019) Einführung in die Höhere Festigkeitslehre, 2nd edn. Springer Vieweg, Berlin, Heidelberg
58. Cowper GR (1966) The Shear Coefficient in Timoshenko's Beam Theory. J Appl Mech 33:335–340. https://doi.org/10.1115/1.3625046
59. Gross D, Hauger W, Schröder J et al (2021) Technische Mechanik 2, 14th edn. Springer Vieweg, Berlin, Heidelberg
60. Öchsner A (2021) Classical Beam Theories of Structural Mechanics, 1st edn. Springer Nature Switzerland, Cham
61. Becker W, Gross D (2002) Mechanik elastischer Körper und Strukturen. Engineering online library. Springer, Berlin
62. Föppl L (1947) Drang und Zwang: Eine höhere Festigkeitslehre für Ingenieure, Band 3, Der ebene Spannungszustand, 1st edn. Leibniz Verlag, München
63. Föppl L (1941) Die unendliche Halbebene bei beliebiger Randbelastung. Sitzungsberichte der mathematisch-naturwissenschaftlichen Abteilung der Bayerischen Akademie der Wissenschaften zu München (1):111–129
64. ANSYS, Inc. (2020) Ansys® Academic Research Mechanical, Release 20.1
65. Braykoff C (2007) Tragfähigkeit kleinmoduliger Zahnräder. Dissertation, Technische Universität München
66. Winter H, Podlesnik B (1983) Zahnfedersteifigkeit von Stirnradpaarungen Teil 1: Grundlagen und bisherige Untersuchungen. Antriebstechnik 22:39–42
67. Winter H, Podlesnik B (1983) Zahnfedersteifigkeit von Stirnradpaarungen Teil 2: Einfluss von Verzahnungsdaten, Radkörpern, Linienlast und Wellen-Naben-Verbindung. Antriebstechnik 22:51–58
68. Winter H, Podlesnik B (1984) Zahnfedersteifigkeit von Stirnradpaarungen Teil 3: Einfluss der Radkörperform auf die Verteilung der Einzelfedersteifigkeit und der Zahnkraft längs der Zahnbreite. Antriebstechnik 23:43–49
69. Daffner M (2018) Validierung von Verformungsberechnungen im System Zahnrad-Welle-Lager-Gehäuse. Dissertation, Technische Universität München
70. Daffner M, Otto M, Stahl K (2017) Method of measuring the load distribution of spur gear stages. JAMDSM. https://doi.org/10.1299/jamdsm.2017jamdsm0076
71. Weinberger U (2021) FVA-Nr. 30/X – Heft 1433 – Erweiterung RIKOR. Forschungsvereinigung Antriebstechnik e.V., Frankfurt/Main
72. Weinberger U, Otto M, Stahl K (2020) Closed-form calculation of lead flank modification proposal for spur and helical gear stages. J Mech Des. https://doi.org/10.1115/1.4045396
73. Geiser H, Schinagl S (1996) Messung der Zahnsteifigkeit eines geradverzahnten Stirnrades und Vergleich mit FEM und Berechnungen nach Weber/Banaschek: FZG Bericht. NR 2064:1–52